frontiers
in Physics

Smart Dielectric Barrier Discharge Plasma Decontamination: Spatially Targeted Decontamination With Actuated Ozone Distribution

Bhaswati Choudhury [1,2,3,4]*, Sherlie Portugal [1,2,5,6], Subrata Roy [1,2,3], Emma Mastro [1,4] and Judith A. Johnson [1,2,4,6]

[1]Applied Physics Research Group, University of Florida, Gainesville, FL, United States, [2]SurfPlasma, Inc., Gainesville, FL, United States, [3]Department of Mechanical and Aerospace Engineering, University of Florida, Gainesville, FL, United States, [4]Emerging Pathogens Institute, University of Florida, Gainesville, FL, United States, [5]School of Electrical Engineering, Technological University of Panama, Panama City, Panama, [6]Department of Pathology, Immunology and Laboratory Medicine, University of Florida, Gainesville, FL, United States

This study introduces spatially targeted decontamination using a synergistic combination of dielectric barrier discharge (DBD) flow actuation and ozone generation. Here, we relate the spatial distribution of local microbial decontaminations in an enclosure to that of local ozone concentrations caused by DBD ozone generation and flow actuation using two reactors with contrasting flow actuation, the Fan and Comb reactors, run at equal power of 1 ± 0.03 W for 3.5 min. Deviations in ozone concentrations and reductions of *Escherichia coli* on contaminated coupons over two planes were used to quantify the utilization capacity of the generated ozone to simultaneously disinfect regions of a surface placed in the planes. Results show that uniform ozone consumption by a contaminated target, i.e., targeted decontamination, lowers ozone requirements, exposure times, and reactor energy consumption for its disinfection. Furthermore, a significant positive correlation was found between local decontamination and ozone concentrations with Pearson's correlation, ρ (34) = 0.64; $p < 0.001$. Simulated ozone distribution using an experiment integrated simulation method, governed by DBD reactor geometry induced flow actuation and ozone reaction rates, is also presented for predicting DBD actuated spatial decontamination distribution. Our study shows an innovative approach of applying DBD plasma reactors for decontamination using flow actuation and ozone generation to achieve targeted killing with maximized ozone utilization lowering overall ozone dosage requirements, energy requirements, and exposure times.

Keywords: plasma, decontamination, ozone, flow actuation, sterilization, dielectric barrier discharge

1 INTRODUCTION

The advent of advanced materials and disinfectant resistant microorganisms, along with the global challenge of environmental pollution, have called for alternative decontamination technologies that can overcome disadvantages of high processing temperatures, long exposure times, harsh chemicals, toxic residuals, and material incompatibility [1–5]. Examples of such need of alternative approaches include minimizing a) the damage of heat-sensitive materials and material alteration with thermal

and chemical treatments in the biomedical and aerospace industry [6, 7] and b) deterioration in food nutrition with traditional processing methods [4]. This paper investigates and demonstrates the unique capability of a promising alternative decontamination method—dielectric barrier discharge (DBD) [6]—in achieving desired decontamination distribution with actuation, i.e., spatially targeted decontamination. The paper also discusses the implications of this unique feature in advancing DBD decontamination by lowering energy consumption, ozone dosage, and exposure times required for decontamination.

Literature shows that DBD-generated low-temperature plasma (LTP) is a potential alternative solution for decontamination in food preservation, medical device industry, clean room facilities, and planetary protection [1, 2, 4, 6–8], with advantages of short exposure times, low temperatures, material compatibility, and no organic residuals [1, 4, 6–9]. Despite these advantages, applications of DBD decontamination have been limited by high-power consumption, bulky equipment, and toxic ozone residuals [7–10]. Although some low-power LTP configurations like plasma pencils exist, they are mostly used in applications like wound healing where small areas are to be disinfected [11]. Among existing DBD configurations available for decontamination of large items, surface DBD (SDBD) is unique due to its design flexibility, surface compliance, easy setup, and inherent flow actuation capability [1, 9, 11]. The SDBD is formed when an AC voltage is applied across two electrodes separated by a dielectric barrier. When the strength of the resulting electric field is above the dielectric strength of the medium, the medium ionizes. This leads to the generation of reactive species, UV photons, and electrohydrodynamic forces [9]. When the medium is air, reactive oxygen and nitrogen species (RONS) form with a mixture of metastably charged oxygen, singlet oxygen, ozone, hydroxyl radicals, and nitrogen compounds that can exert antimicrobial property by killing a broad range of pathogens. Specifically, superoxide, hydrogen peroxide, hydroxyl radical, singlet oxygen, and nitrogen oxides (NOx) have shown to have reliable disinfecting kinetics [12, 13] making SDBD treatment a viable disinfection method. SDBD treatment of objects involves direct contact with discharge or indirect contact through reactive species. Unlike direct contact, indirect DBD treatment makes it possible to treat spaces obscured from direct view (for example, of UV light). A thorough study on the reaction kinetics and antimicrobial pathways of RONS is highly warranted and, to our knowledge, is yet to be done.

Among all DBD-generated species, ozone is a known contributor in microbial inactivation due to its high oxidation potential and prolonged existence compared to other species [14, 15]. Microbial inactivation using ozone has been studied extensively by many researchers over the years against various pathogens [16–19]. The mechanism of ozone inactivation of microorganisms occurs in three steps: destruction of cellular surface, leakage of cellular components, and cell lysis [19]. The cell surface is thought to be the primary target of inactivation. Research studies suggest that two major oxidation mechanisms are involved in ozone microbial inactivation: a) oxidation of sulfhydryl groups and amino acids of enzymes, peptides, and proteins to shorter peptides and b) oxidation of polyunsaturated fatty acids to acid peroxides [17]. Ozone oxidation reactions with components of the cell surface cause its degradation. This results in disruption of the cell surface and leakage of cellular components. Progressive oxidations result in cell lysis leading to inactivation. Nucleic acids of the cells are also destroyed by ozone oxidations. Furthermore, it has been reported that ozone destroys viral RNA and protein coats by alteration of polypeptide chains [20].

Although a lot of studies exist on inactivation mechanisms of DBD-based RONS (specifically ozone) and its potential to kill a wide variety of pathogens including bacteria, virus, and disinfectant-resistant microorganisms [14–22], distributed decontamination through ozone generated and distributed by DBD, without the aid of an external distributing agent, has not been investigated yet to the best of our knowledge. The scientific question addressed here is whether such distributed decontamination can be achieved with a synergistic combination of DBD flow actuation and ozone generation. If this is feasible, DBD reactors for indirect treatment can be developed with an in-built distribution mechanism, without adding external mixing enhancers, for maximum utilization of the generated ozone while achieving targeted decontamination. Maximizing ozone utilization will, in turn, lower required exposure times, ozone requirements, residual ozone, and energy requirement. Additionally, an inbuilt distribution mechanism without adding external distributing components will help lower equipment size. Such DBD reactors designed for decontamination with inbuilt ozone mixing and distributing capabilities can help mitigate limitations of high-energy consumption, bulky equipment, and toxic ozone residual levels associated with DBD treatment for a wide range of decontamination applications including food preservation, sterilization of surgical tools, air purification systems, and tool sterilization in space explorations for end-to-end sample return and ground-based contamination control.

This research investigates spatial variation in microbial decontamination inside an enclosure caused by a SDBD reactor and examines its relation to SDBD-generated ozone distributed by plasma actuated flow. The relation between local microbial decontaminations and local ozone concentrations in an enclosure is also examined. While a range of RONS species may be important in microbial disinfection, due to the limitation of the instrumentation and experimental method used for this paper, only the spatial measurement of ozone generated from two specific designs of SDBD reactors is considered. It is assumed that the distribution of other RONS species will be locally proportional to the ozone distribution since they are generated from the same reactor. The two SDBD reactor designs used in this study are the comb-shaped reactor and the recently developed fan-shaped reactor [23]. These reactors were chosen based on the contrasting flow patterns generated by them, which was expected to result in contrasting ozone distribution and resulting decontamination distribution. The
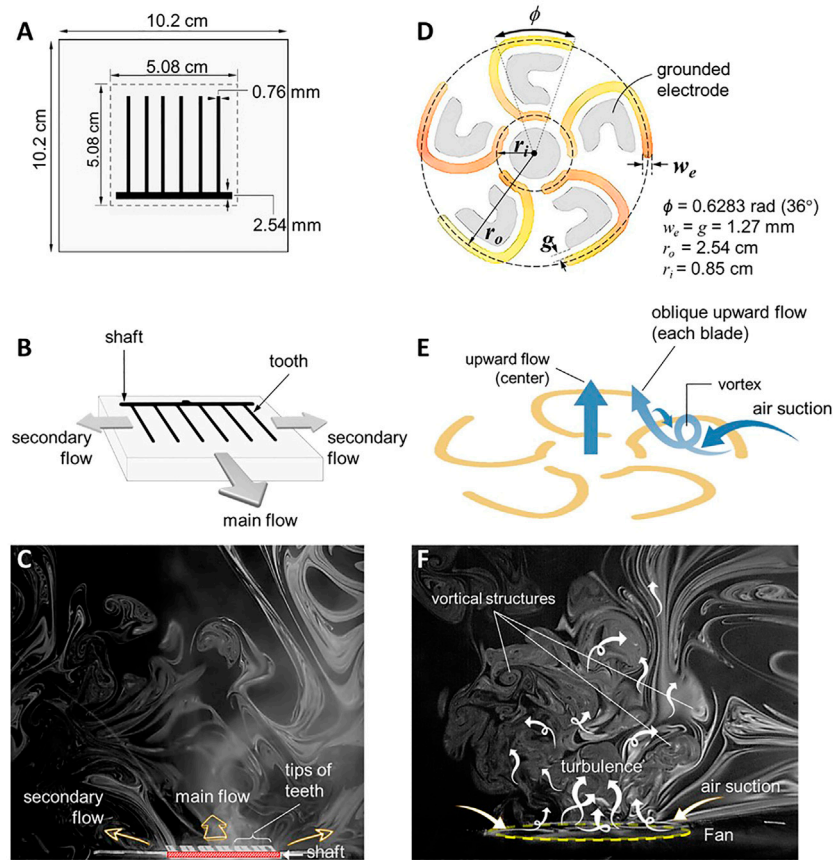
FIGURE 1 | Illustration of comb and fan reactors with flow visualizations. **(A)** Comb reactor—solid and dashed lines representing the exposed and ground electrodes, respectively. **(B)** Comb's characteristic flow—arrows show three wall jets with the dominant one in the direction from the shaft toward the teeth tips. **(C)** Smoke flow visualization of comb's reactor actuated flow. **(D)** Fan reactor—colored and gray areas representing the exposed and ground electrodes, respectively. **(E)** Fan's characteristic flow of each blade and the center. **(F)** Smoke flow visualization of the fan reactor actuated flow—the fan blades interact to form vortical structures resulting in overall conical flow thrusted upward from the reactor base.
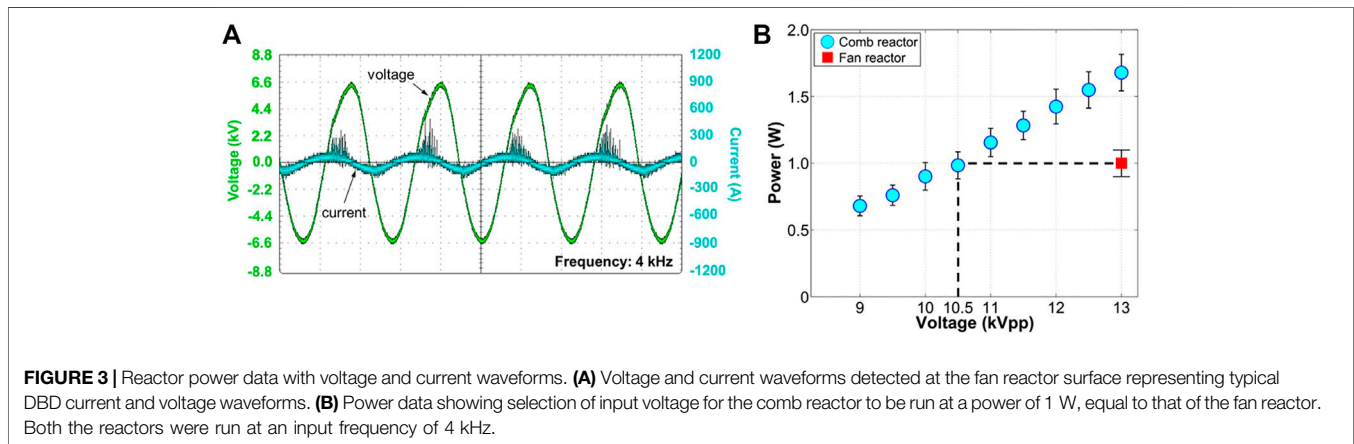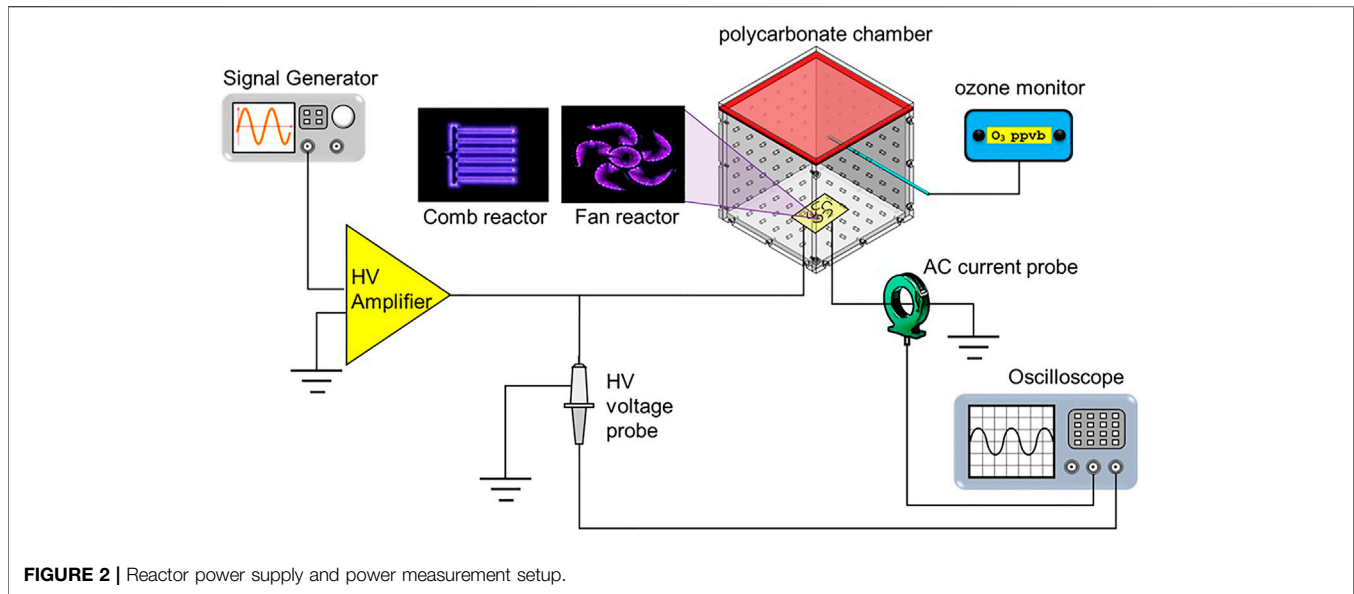
core idea is to synergistically employ flow actuation and ozone generation by SDBD reactors to simultaneously generate and distribute ozone for targeted decontamination with maximum ozone utilization. Distribution in SDBD-generated ozone resulting from SDBD actuated flow is referred to as SDBD actuated ozone distribution in this paper. Additionally, decontamination data resulting from SDBD actuated ozone distribution are referred to as SDBD actuated decontamination distribution. Results show that SDBD actuated ozone distribution lowers ozone requirements and corresponding energy consumption and exposure times to achieve desired decontamination, revealing the full potential of DBD decontamination. Furthermore, a Pearson's correlation test showed significant positive correlation between local decontamination inside an enclosure and ozone available at that point for a fixed exposure time. Additionally, an experiment integrated simulation method is discussed for designing SDBD reactors for targeted decontamination using available SDBD body force distribution models and experimental ozone generation and decomposition rates [24, 25].

2 MATERIALS AND METHODS

This section is organized as a) experimental design for studying spatial distribution of microbial decontamination in a chamber, b) experimental design for studying spatial distribution of ozone concentrations in a chamber, c) numerical design for simulation of ozone distribution and flow field generation in the chamber, and d) statistical analysis.

2.1 Experimental Design for Studying Spatial Distribution of Decontamination in a Chamber

The experimental setup and procedure explained in this subsection is used to examine microbial decontamination distribution in a chamber using two SDBD reactor designs. For these experiments, inoculated agar plates and coupons are examined for decontamination by placing them at selected locations inside the chamber fitted with an SDBD reactor at the base.

FIGURE 2 | Reactor power supply and power measurement setup.

FIGURE 3 | Reactor power data with voltage and current waveforms. **(A)** Voltage and current waveforms detected at the fan reactor surface representing typical DBD current and voltage waveforms. **(B)** Power data showing selection of input voltage for the comb reactor to be run at a power of 1 W, equal to that of the fan reactor. Both the reactors were run at an input frequency of 4 kHz.

2.1.1 Reactor Configurations and Power Setup

The reactor shapes used in this study are the common comb and the fan; both SDBD designs yield contrasting flow actuation capabilities. **Figure 1** shows the details of the two reactors along with smoke flow visualization of the flow generated by them. **Figures 1A,D** illustrate the schematic and dimensional representation of the comb and fan reactors. For both the reactors, the dielectric barrier had a total area of 10.2 cm × 10.2 cm and was made of 0.76-mm-thick hydrocarbon-ceramic (RO4350B) material. The electrodes were made of 35-μm-thick copper layers. **Figures 1B,C** show the comb reactor generating three wall jets, with the dominant one being in the direction from the shaft toward the teeth tips, while remaining almost parallel to the surface of the reactor. The fan, on the other hand, produces an overall conical flow thrusted upward from the reactor base as shown in **Figures 1E,F**; [23]. In contrast to the wall jets generated by the comb reactor, which stay close to the reactor surface, the fan reactor suctions the surrounding gas and pushes it away and

upward from the reactor's surface. Such flow is characterized by chaotic vortical structures resulting from the combination of individual flows from the five blades and the center of the fan, and which are shown in **Figure 1E**.

The reactors were powered inside the experimental chamber (polycarbonate chamber) using the power supply and measurement setup shown in **Figure 2**. An AC voltage wave of amplitude 6.5 kV, i.e., peak-to-peak input voltage of 13 kVpp (kV peak-to-peak), was fed to the fan reactor. **Figure 3A** shows the voltage and current waveforms detected on the reactor surface during plasma formation. These represent typical waveforms of DBD voltage and current. SDBD microdischarges occur during the voltage rise in the positive half of the cycle and during the descent in the negative half of the cycle. The presence of discharges during the positive cycle generates current spikes of large amplitude and short duration as shown in **Figure 3A**. Some researchers [26–28] have studied these discharges at a microscopic level, revealing that their structure corresponds to streamers with erratic propagation paths in continuous contact with the surface of the

dielectric. During the negative cycle, on the other hand, discharges produce a dense population of current spikes, which are much smaller that the spikes of the positive cycle and barely perceptible in **Figure 3A**, but in average account for more current. At a microlevel, discharges in the negative cycle are comprised by a great number of corona spots that originate at the edge of the exposed electrode and extend over the dielectric surface that from afar produce a uniform or diffuse glow [28–30].

The frequency of the applied voltage was 4 kHz. This frequency was chosen for two main reasons, the first one being that dielectric losses increase with frequency, and unwanted effects like the formation of leaders tend to manifest faster with the increase in frequency than with the increase in voltage [28, 31]. The second reason is that internal slew rate limitations of the high-voltage amplifier used for these experiments (Trek Model 20/20C) degenerated the 13-kVpp voltage waveform into a sawtooth shape for higher frequencies. Therefore, it was decided that the combination 13 kVpp/4 kHz was the optimal compromise between the plasma and ozone generated and the power consumed [25] while maintaining the integrity of the electrical characteristics of voltage and current.

For calculating power consumption of the reactors, an oscilloscope (Tektronix DPO 3014) with recording length set to 1 million points was programmed through a LabVIEW code to collect the voltage and current waveform data every 40 s for 4 min. This was repeated three times for statistical confidence. The collected data were processed in MATLAB to obtain the average power consumed by the reactors, along with the uncertainties, as presented in **Supplementary Data S2**.

The reactors were to be run at equal power for all the experiments to compare decontamination results achieved at same power levels. To achieve this, the fan reactor was first run at peak-to-peak input voltage (kVpp) of 13 kVpp and 4 kHz frequency, resulting in power consumption of 1 ± 0.03 W. This was followed by testing the power consumption of the comb reactor at different voltages, keeping the frequency constant at 4 kHz, until the measured power was equal to that of the fan (see **Figure 3B**). Thus, both the reactors were run at equal power of 1 ± 0.03 W corresponding to following input voltages and frequencies for the fan and comb reactors, respectively: 13 kVpp/4 kHz and 10.5 kVpp/4 kHz.

2.1.2 Test Organism and Preparation of Cultures
Escherichia coli (*E. coli*)—K12 is a Gram-negative, facultative anaerobe with the ability to replicate under very low pressures. This replication ability makes this bacterial species of interest for evaluation of decontamination technologies in various fields [32, 33]. A BSL-1 strain, *E. coli* K12 Strain MSG 123 (**ATCC** PTA-7555), of the bacteria was used for this study.

A loopful of *E. coli*, stored at −80°C in LB (Luria-broth) with 30% glycerol, was streaked onto an LB plate and incubated at 37°C for 18–24 h. Two to four colonies from the plate were inoculated into 3 ml of LB broth and emulsified with a Fisher Scientific® Mini Vortexer Lab Mixer (~1 min) to eliminate clumps and obtain approximately 5×10^7 CFU/ml (colony forming units/ml). The resulting inoculum was used to prepare contaminated agar plates and coupons for testing decontamination achieved by SDBD exposure.
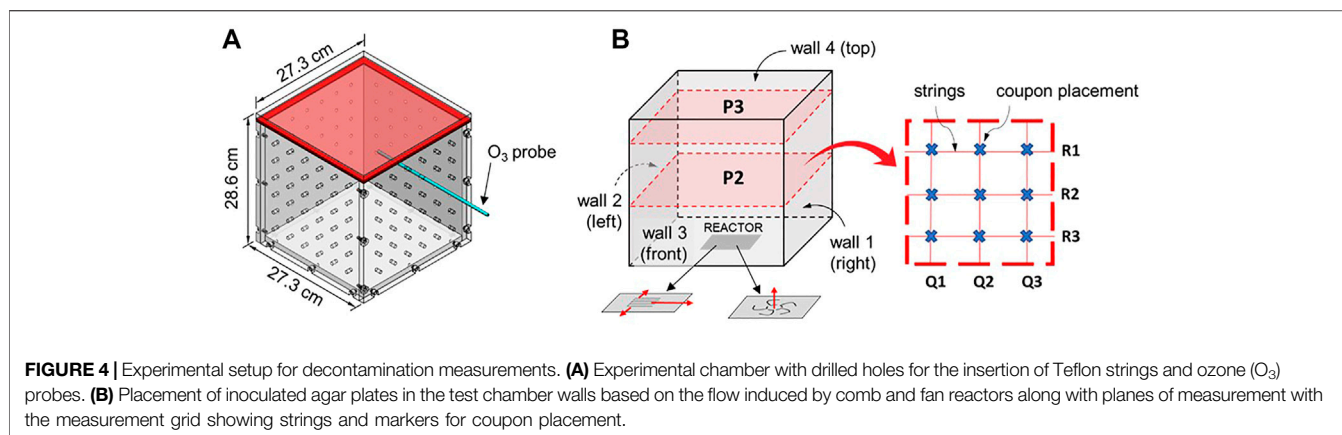
2.1.3 Coupon Material
Whatman Grade 42 Filter paper of 200-μm thickness and 2.5-μm pore size [34] was chosen as the coupon material after testing other sterilized materials like medical gauge and band-aid materials. This selection was made based on the ability of these filter papers to absorb the inoculation volume without changing its shape and convenience of spreading the inoculum uniformly on the paper with the help of a micropipette with less chances of it leaking or spilling. Furthermore, using inoculated filter paper coupons is a technique commercially used to test disinfection methods [35].

2.1.4 Experimental Setup and Procedure
Figure 4 shows the main components of the experimental setup, which includes a Teflon-coated polycarbonate test chamber (27.3 cm × 27.3 cm × 28.6 cm), SDBD reactors, and coupons (or agar plates) inoculated with the prepared inoculum. A polycarbonate chamber was chosen to avoid experimental error due to ozone reaction with chamber walls as polycarbonate is inert to ozone. A total of 36 resealable holes were drilled in each chamber wall to facilitate insertion of a) Teflon strings to suspend inoculated coupons for collecting decontamination data and b) temperature, humidity, and ozone probes for measurements inside the chamber, as shown in **Figure 4A**. The reactor was placed at the center of the base of the chamber with the exposed electrode facing up. All the experiments were performed under atmospheric conditions. Temperature and humidity inside the chamber were monitored with a chart recorder EXTECH Instruments RH520A-NIST. Ozone measurements were not performed simultaneously with decontamination experiments to preserve the ozone amounts used for disinfection inside the chamber. In the beginning of every experiment, the test chamber and all the components inside it were disinfected with 70% isopropyl alcohol to avoid external contamination. Furthermore, at the start of each experiment, it was ensured that ozone concentrations inside the chamber match room-level ozone concentrations.

2.1.4.1 Agar Plate Tests
The extent of difference in local decontamination caused by the reactors at the chamber boundaries, with the selected chamber size and reactor size, was initially examined to substantiate the study of distribution in decontamination inside the chamber. **Figure 4B** illustrates the orientation of reactor placement and four walls of the chamber selected for testing based on the difference in flow induced by the two reactors. LB agar plates inoculated with 10^4–10^5 CFUs/plate of *E. coli* were placed at the wall centers and exposed to the reactors for 4 min. In this context, exposure time is the duration for which the reactor is turned on with the agar plates inside the chamber, while residence time refers to the time the agar plates are left inside after powering off the reactors. To observe distribution in disinfection due to ozone distributed by the two reactor configurations, these experiments were run with zero residence time. Three inoculated agar plates were placed outside the chamber for the duration of the experiment as control and are referred to as control or unexposed plates. The exposed and unexposed agar plates are

FIGURE 4 | Experimental setup for decontamination measurements. **(A)** Experimental chamber with drilled holes for the insertion of Teflon strings and ozone (O₃) probes. **(B)** Placement of inoculated agar plates in the test chamber walls based on the flow induced by comb and fan reactors along with planes of measurement with the measurement grid showing strings and markers for coupon placement.

incubated at 37°C for 18–24 h after each experiment, and the difference in the CFU count of the plates was used to measure the reduction in bacterial count. Decontamination or killing of bacteria is expressed as logs of reduction in CFU/plate.
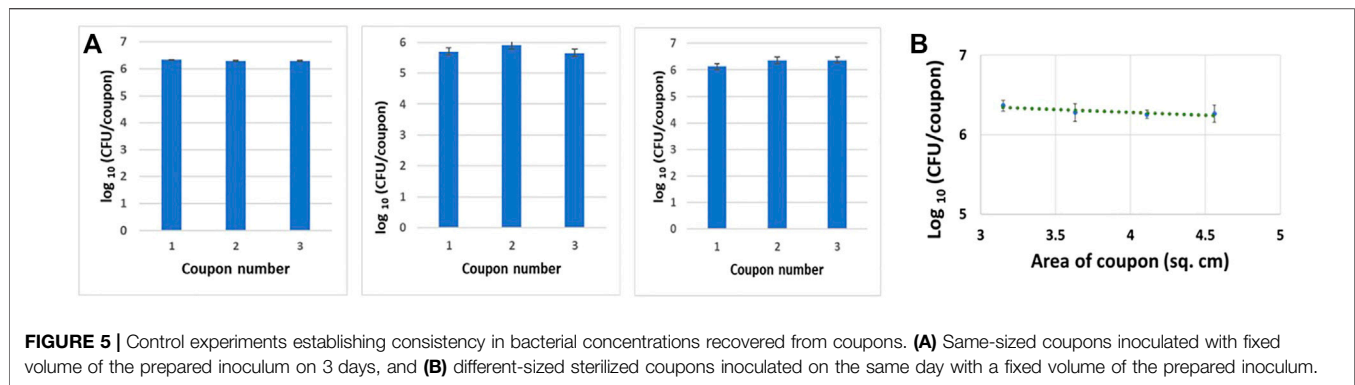
2.1.4.2 Coupon Tests

The agar plate tests were followed by coupon testing to examine SDBD actuated decontamination distribution inside the chamber. The coupons were first sterilized by autoclaving them at 121°C in a dry autoclave cycle before all experiments. About 10 µl of the inoculum containing 5×10^7 CFU/ml was spread on each sterile coupon used in the experiment to get 5 to 6 logs of CFU/coupon. For each experiment, 18 inoculated coupons were placed in a 3 × 3 measurement grid in two planes—P2 and P3 (11.5 and 18.5 cm from the reactor surface)—inside the chamber as shown in **Figure 4B**, followed by SDBD exposure of 3.5 min. Three inoculated coupons were placed outside as control and referred to as unexposed coupons. About $4 \pm 0.4 \, \text{cm}^2$ sized coupons were used based on control experiments performed to establish consistency in CFUs per coupon for areas between 3 and 5 cm² when using equal inoculation volume. The control experiments are explained in the next section. The coupons were suspended inside the test chamber using sterile Teflon-coated strings (0.1-mm diameter) using the resealable holes in the chamber. Teflon was used to avoid ozone loss due to reaction with or deposition on the strings. At the end of the experiments, postprocessing was performed on the coupons to get the bacterial counts (CFU/coupon). For postprocessing, the exposed and unexposed coupons were vortexed thoroughly in 4 ml PBS and serial dilutions spread on LB agar plates followed by incubation at 37°C for 18–24 h. Decontamination achieved was measured by the difference in CFU/coupon in the exposed and unexposed (control) coupons. Five repeats of each experiment were performed to establish repeatability. The effect of bacterial inactivation on the coupons due to drying of the coupons was eliminated by control experiments performed on agar plates. Following each experimental run, the residual ozone inside the test chamber was removed using a vacuum cleaner till room-level ozone concentrations were obtained and the setup was disinfected. Additionally, a gap of at least an hour was maintained between two experiments with the chamber lid

open to ensure that chamber conditions correspond to atmospheric conditions.

2.1.5 Control Experiments

Control experiments were performed to ensure correct quantification of inactivation of bacteria due to SDBD reactor exposure. Two sets of control experiments are performed. The first set involved testing of the agar plates and sterilized coupons for external contamination. This was achieved by testing bacterial growth on the coupons and agar plates left inside the chamber for the experimental time periods without inoculating them or exposing them to the reactors. No bacterial growth on the plates and coupons ruled out error due to external contamination. This was done to ensure that the inactivation achieved in these experiments are solely dependent on SDBD plasma exposure and is not affected by other environmental factors related to the experimental procedure like the duration of the experiment and human influence during preprocessing or postprocessing. The second set of control experiments involved establishing consistent bacterial concentrations for same- and different-sized sterilized coupons inoculated with a fixed volume of the prepared inoculum. Three repeats of the control experiments were performed on three different days with three same-sized coupons being tested in each repeat. The results obtained are shown in **Figure 5A** with error bars based on standard deviation. The data obtained showed that inoculating same-sized coupons with the same amount of the prepared inoculum on different days resulted in consistent bacterial count per coupon with a maximum variation of 0.12 $\log_{10}$(CFU/coupon). Experiments were also performed to examine bacterial count on coupons of different area inoculated with the same amount of the prepared inoculum. For these experiments, 0.01 ml of the prepared inoculum was spread on sterilized coupons of area 3.15, 3.63, 4.11, and 4.56 cm². The data obtained, shown in **Figure 5B**, showed that inoculating different-sized coupons with the same amount of the prepared inoculum resulted in consistent bacterial count per coupon with a maximum variation of 0.05 $\log_{10}$(CFU/coupon). Three repeats were performed for each data point shown in **Figure 5**.

FIGURE 5 | Control experiments establishing consistency in bacterial concentrations recovered from coupons. **(A)** Same-sized coupons inoculated with fixed volume of the prepared inoculum on 3 days, and **(B)** different-sized sterilized coupons inoculated on the same day with a fixed volume of the prepared inoculum.

2.2 Experimental Design for Studying Spatial Distribution of Ozone Concentrations in the Chamber

The experimental setup and procedure explained in this subsection was used to examine ozone distribution in the previously described experimental chamber using the two SDBD reactors. Similar to the decontamination experiments, ozone data were collected for planes P2 and P3 inside the chamber in a finer measurement grid of 6×6 points over 5 min. Reactor placement was kept analogous to the decontamination experiments. Ozone was measured by inserting a probe through holes in the chamber walls and placing it at measurement grid points in the 3 planes as shown in **Figure 4A**. The probe was connected to the 2B Technologies Model 202 Ozone Monitor™, which works based on UV light absorption at 254 nm, to measure the ozone. The accuracy of the monitor is 1.5 ppb or 2% of the reading [36]. Measurement at each grid point was taken separately to minimize the error due to negative pressure caused by simultaneous measurements at multiple grid points in the same chamber.

Ozone data were additionally collected at Plane P1, 3.5 cm from the reactor base, to understand the distribution of the ozone near the plasma formation and ozone generation area at the reactor surface. At least 3 repeats of data were collected for statistical confidence. Experimental ozone distribution data at P1 were also used to validate the numerically simulated ozone distribution at plane P1 using ozone generation and flow actuation of the SDBD reactors. Note that decontamination data at plane P1 were out of scope for this experimental setup due to the possible effect of inoculated coupon placement near the reactor surface on the reactors and vice versa.

Test chamber conditions for decontamination data and ozone data collection: Measurements of ozone concentrations inside the test chamber prior to starting every experiment were checked to be in the room-level ozone. The temperature inside the chamber remained at 23.0 ± 3.0°C for all the experiments. The relative humidity levels varied in the range 72.0 ± 2.0%.

2.3 Numerical Design for Simulation of Ozone Distribution and Flow Field Generation

ANSYS Fluent [37] is used for simulating the actuated flow and the ozone distribution generated by the two reactor configurations near the reactor surface. The simulations were performed for the experimental box of size 27.3 cm × 27.3 cm × 28.6 cm described in the previous section. This section describes modeling of the body force and ozone generated by the SDBD reactor configurations included in the flow governing equations as momentum and mass source terms, respectively. Ozone decomposition was included in the ozone mass source term.

The simulations assumed incompressibility based on atmospheric conditions and low fluid speeds (<1 m/s) observed in experiments. Wall boundary conditions were set to represent the experimental chamber walls with negligible penetration, negligible diffusive flux, and negligible surface roughness. Initial flow conditions were set to ambient room conditions. Since the goal of this study was to obtain the overall flow produced by the reactor configurations for simulating the resulting ozone distribution, the ensemble-averaged flow governing equations were solved using the RANS (Reynolds-Averaged Navier–Stokes equations) module. The SDBD body force model used in this study is obtained from the study performed by Singh and Roy [24] on simulating the effects of plasma actuators. Lines of actuation used in incorporating the body force model for the two reactors as a momentum source were identified based on plasma literature on flow actuation [38, 39].

For simulating the ozone distribution in the chamber, SDBD ozone generation and ozone decomposition terms were incorporated into the flow simulations. This was performed by solving additional species transport equations along with the flow equations simultaneously at each time step. Three species (ozone, oxygen, and nitrogen) were considered in the simulations to get spatial and temporal ozone distributions by the two reactor configurations. The species transport equation is given by the following advection–diffusion equation:

$\frac{\partial C}{\partial t} + \nabla \cdot (\boldsymbol{u}C) - \nabla \cdot (D\nabla C) = S$; C = species concentration, $\boldsymbol{u}$ = velocity, D = molecular diffusivity of the species molecules, and S = source term for the species.

Initial mixture fractions were set to 0.23, 0, and 0.77 for oxygen, ozone, and nitrogen, respectively, to represent atmospheric composition.

Ozone formation with gas discharges has been extensively studied throughout the years. Some of the notable works in this area were homogeneous ozone formation models [40], models involving simple avalanche [41], corona-discharge-based ozone

formation [42], discharge structure modeling [43], and DBD-based ozone formation [44]. Due to the time scales of ozone formation reactions, such studies are usually focused on time scales of micro- to milliseconds [38]. Because of this, ozone distribution simulations focusing on ozone formation mostly look at smaller time and length scales. Ozone distribution in the context of photochemical air simulation studies that employ ozone generation source models to study ozone distribution in model rooms or ozone removal is more relevant to this study [45–47]. Thus, the source term in the ozone transport equations was modeled similar to model room studies [47] to include ozone generation and decomposition rates, shown in the equation below.

$S = s(t) - kC$; C = concentration of ozone (ppb), s(t) = rate of ozone generation (ppb/min), and k (ppb/min) = rate constant for ozone decomposition.

s(t) was calculated based on the experimental ozone generation rate near the reactor surface (1.8×10^{-8} kg/m^3-s) and applied to the corresponding cells of the computational domain. An equivalent sink term [-s(t)] for oxygen was applied in the oxygen species transport equation for mass conservation inside the chamber. The overall reaction rate of ozone decomposition is considered instead of elementary reactions involved in the decomposition process. This reaction rate is obtained from experimental data acquired by Portugal et al. [25] showing an exponential decay of ozone concentrations with time as shown in the following equation.

$$O_3(t) = A \exp(-0.005t); \text{ t = time and A = Constant}$$

The above decomposition reaction rate shows a first-order reaction mechanism for decomposition of ozone to oxygen in air and is explained by the similar functional relationship observed with respect to the reaction rate equation derived from differential rate expression governing chemical reactions for a first-order reaction given in the equation below [48].

$r(t) = r_0 \exp(-kt)$; r(t) = concentration of the reactant at time t, r_0 = its initial concentration, k = reaction rate, and t = time.

Comparison of the experimentally obtained ozone decomposition rate equation and the general first-order reaction rate equation was used to obtain the reaction rate (k) for the bimolecular decomposition of ozone (O_3) to oxygen (O_2) in air.

$$2O_3 \xrightarrow{k} 3O_2$$
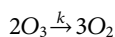
Ozone decomposition in air has been extensively studied by various scientists, and many bimolecular as well as atomic reactions have been proposed to explain the decomposition mechanism [49, 50]. Glissman and Schumaker [50] found that atomic reactions are significant only when dealing with very small amounts of ozone concentrations. In these simulations, we assume the ozone to oxygen decomposition to be a direct bimolecular reaction. Since the reaction rate is obtained experimentally, it is safe to assume that the reaction rate of this direct bimolecular reaction incorporated in the simulations is the resultant reaction rate that includes all the intermediate elementary reactions involved in the decomposition process.

2.4 Statistical Analysis

Each of the decontamination data measured over 18 points (two 3×3 grids) in two planes of the chamber was repeated 5 times, i.e., $n = 5$, to gain statistical confidence. The total uncertainty of decontamination measurements included the uncertainty due to variations in the results of each repeated experiment and was quantified using standard deviations arising from variation in repeats. Additionally, each ozone measurement was repeated at least 3 times for statistical confidence. The total uncertainty of ozone measurements includes the uncertainty due to variations in the results of each repeated experiment and error due to the ozone monitor.

A bivariate Pearson's correlation [51], with one-sided test, was used to test whether there is a statistically significant positive correlation between local ozone concentrations and resulting decontamination. Thus, the null and alternate hypotheses tested are H_0: $\rho \le 0$ and H_A: $\rho > 0$, respectively. Here, ρ is the Pearson's correlation value indicating the following: $\rho \le 0$ implies that there is a negative correlation or no correlation, while $\rho > 0$ means that there is a positive correlation. The p-value in this test indicates whether the resulting correlation is statistically significant, and N represents the sample size. Alpha indicates the significance level, i.e., the probability of rejecting the null hypothesis when it is true. In this study, alpha (α) was set to 0.001 representing a 0.1% risk of concluding that there exists a positive correlation when there is none. N represents the sample size or the number of data points. Thus, a Pearson's correlation value ρ (N) > 0 with $p < \alpha$ would indicate a significant positive relationship between local decontamination achieved at a point inside a chamber and corresponding ozone concentration reaching that point.
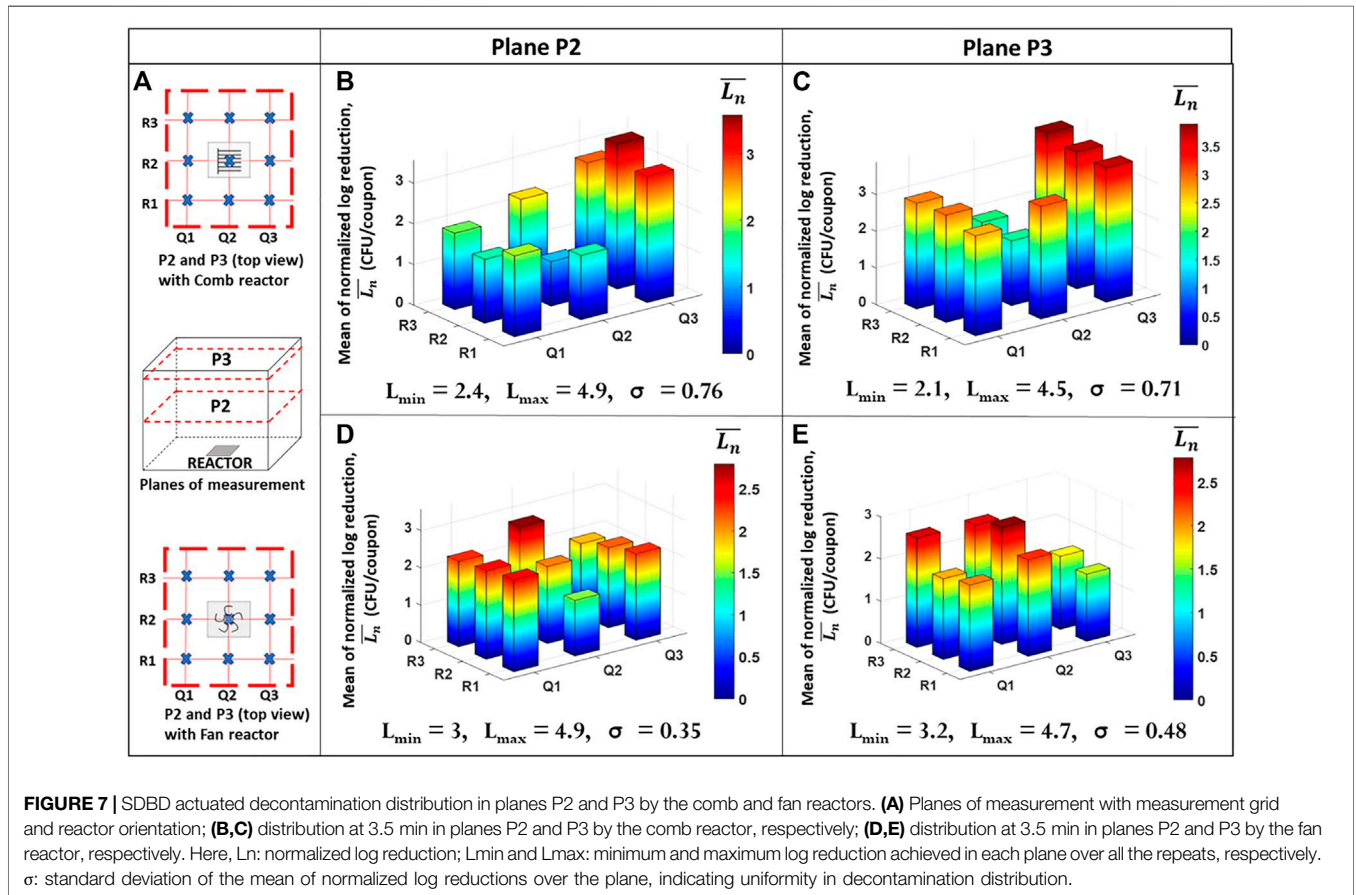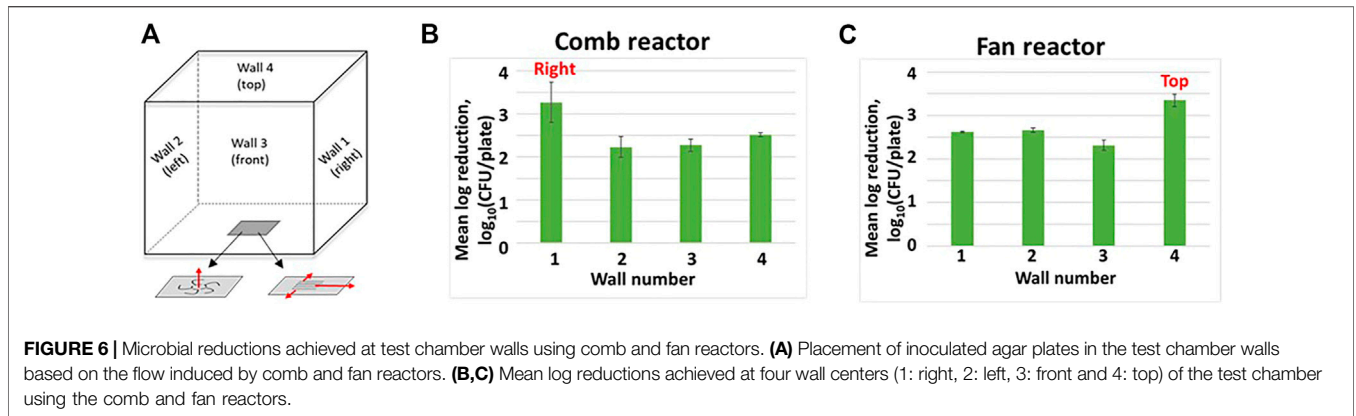
3 RESULTS

Spatial distribution in local decontamination inside a chamber caused by two contrasting SDBD reactor configurations, referred to as SDBD actuated decontamination distribution, is presented. This is then related to SDBD actuated ozone distribution (spatial distribution of local ozone concentrations) and flow patterns observed through experiments and simulations. Finally, targeted decontamination is discussed through SDBD reactor designs based on numerically predicted ozone distribution. Additionally, a significant positive correlation is established between local decontamination inside an enclosure and ozone available at that point for a fixed exposure time. Note that microbial decontamination is referred to as decontamination in the rest of the document to indicate that SDBD actuated decontamination can be used to achieve both disinfection (reduction of microbial contamination to acceptable levels) and sterilization (complete killing of all microbes) based on the application requirements.

3.1 SDBD Actuated Decontamination Distribution

Results of initial agar plate tests showing the extent of difference in local decontamination caused by the reactors at the chamber

FIGURE 6 | Microbial reductions achieved at test chamber walls using comb and fan reactors. **(A)** Placement of inoculated agar plates in the test chamber walls based on the flow induced by comb and fan reactors. **(B,C)** Mean log reductions achieved at four wall centers (1: right, 2: left, 3: front and 4: top) of the test chamber using the comb and fan reactors.

FIGURE 7 | SDBD actuated decontamination distribution in planes P2 and P3 by the comb and fan reactors. **(A)** Planes of measurement with measurement grid and reactor orientation; **(B,C)** distribution at 3.5 min in planes P2 and P3 by the comb reactor, respectively; **(D,E)** distribution at 3.5 min in planes P2 and P3 by the fan reactor, respectively. Here, L_n: normalized log reduction; L_{min} and L_{max}: minimum and maximum log reduction achieved in each plane over all the repeats, respectively. σ: standard deviation of the mean of normalized log reductions over the plane, indicating uniformity in decontamination distribution.

boundaries, to substantiate the study of distribution in decontamination inside the chamber, are shown in **Figure 6**. **Figure 6A** shows the reactor orientation and **Figures 6B,C** show the mean log reduction achieved with three repeats for each wall. The comb reactor resulted in maximum decontamination at Wall 1 (right) with an average of > 1 log reduction more compared to the other walls tested (Walls 2, 3, and 4). Significant (>1 log) difference in decontamination achieved by the reactors at the chamber walls indicated possible distributed decontamination inside the chamber.

Distribution in local decontamination, i.e., SDBD actuated decontamination distribution, achieved with 3.5 min of exposure time was obtained through 5 repeated measurements over nine grid points: Q1R1, Q1R2, Q1R3, Q2R1, Q2R2, Q2R3, Q3R1, Q3R2, and Q3R3, at each plane for both the reactors as shown in **Figure 7A**. For accurate averaging over repeats with small variations in initial CFU/coupon, log reduction (L) for each repeat was normalized (L_n) with the minimum value (L_{min}) obtained for that repeat and set to 1. This allowed for the calculation of mean log reduction ($\overline{L_n}$) of the normalized data

at each measurement point for 5 repeats. The deviations (σ) in the mean log reductions obtained in P2 and P3 measurement grid were used to indicate uniformity in the decontamination distribution in those planes, i.e., higher deviations indicate less uniform distribution. Note that the decontamination distribution in plane P2 best indicates the effect of SDBD actuated ozone distribution due to minimal wall-flow interactions.

Figures 7B–E show SDBD actuated decontamination distribution over planes P2 and P3 by the comb reactor and the fan reactor after an exposure time of 3.5 min. Note that $\overline{L_n}$ values over the measurement grid in each plane is a relative measure to the minimum log reduction (L_{min}) obtained over that plane. L_{min} and L_{max} values for a plane indicate the minimum and maximum log reduction, respectively, obtained in that plane by each reactor based on average of 5 repeats.

3.1.1 Decontamination Distribution in Plane P2

The comb reactor resulted in higher microbial reductions (4–5 log) along line Q3 compared to other points (see Figure 7B), with a maximum of 4.9 ± 0.5 log reduction ($\overline{L_n}$ = 3.6 ± 0.8) at point Q3R2 and minimum of 2.4 ± 0.5 log reduction ($\overline{L_n}$ = 1 ± 0.2) at the central point, Q2R2. The fan reactor resulted in overall higher microbial reductions (4–5 log) with a maximum of 4.9 ± 0.4 log reduction ($\overline{L_n}$ = 2.8 ± 0.6) at Q2R2 and minimum of 3 ± 0.4 log reduction ($\overline{L_n}$ = 1.1 ± 0.2) at Q2R1, both points lying at the center line of the plane. The resulting distribution in decontamination is depicted in Figure 7D. Here, the comb and fan reactors resulted in deviations of 0.76 and 0.35, respectively. Thus, the fan reactor would decontaminate a surface with 5 log CFU/in.[2] placed in plane P2 more uniformly and in less time than the comb reactor. In other words, if a surface to be disinfected by the comb reactor were to be placed in P2, it would be disinfected unevenly for the exposure time of 3.5 min resulting in lower overall disinfection thereby requiring higher ozone dosage and longer exposure for disinfection of all regions. In comparison, the surface in P2 would be disinfected more uniformly by the fan reactor for the exposure time of 3.5 min, resulting in higher overall disinfection of the surface than the comb reactor.

3.1.2 Decontamination Distribution in Plane P3

The comb reactor resulted in a more uniform distribution of decontamination levels in plane P3 than P2 with higher microbial reductions (4–5 log) along most points except for Q2R2 and Q2R3 with a maximum of 4.5 ± 0.5 log reduction ($\overline{L_n}$ = 4 ± 0.5) at Q3R3. The fan reactor resulted in similar uniform decontamination distribution in plane P3 compared to P2 with relatively higher microbial reductions (4–5 log) along the central line Q2. A maximum of 4.7 ± 0.6 log reduction ($\overline{L_n}$ = 2.9 ± 0.8) was observed at point Q2R2. The resulting distribution in decontamination by the two reactors is depicted in Figures 7C,E, with deviations of 0.48 and 0.71 caused by the fan and comb reactors, respectively. Like plane P2, these results indicate that the fan reactor would decontaminate a surface placed in plane P3 more uniformly and in less time than the comb reactor.

SDBD actuated decontamination distributions differ in the two planes based on the ozone distribution generated by the two reactor designs. The ozone distribution is, in turn, caused by the

differences in flow actuation generated by the two reactor designs. This is explained with experimental and simulated data in the subsequent sections.

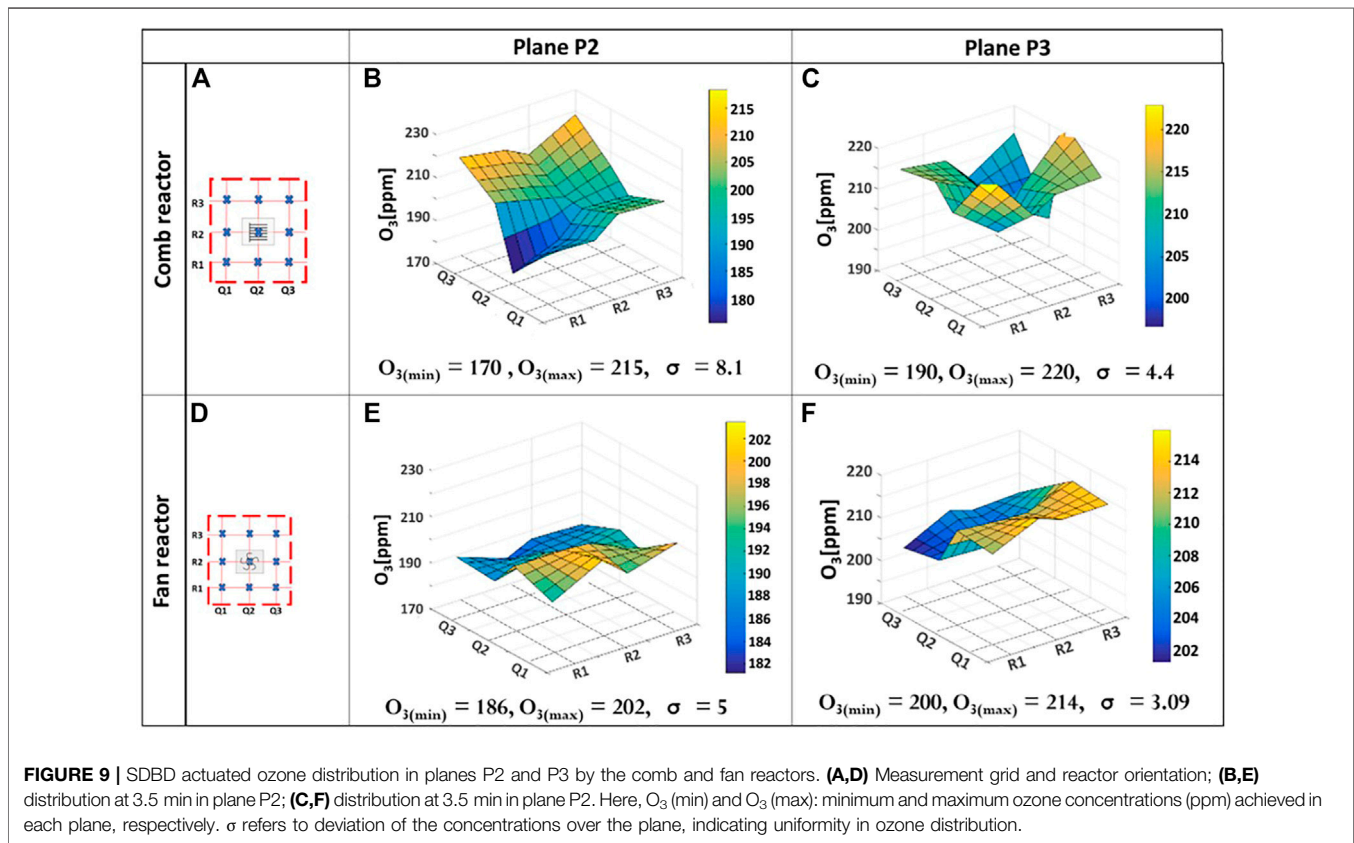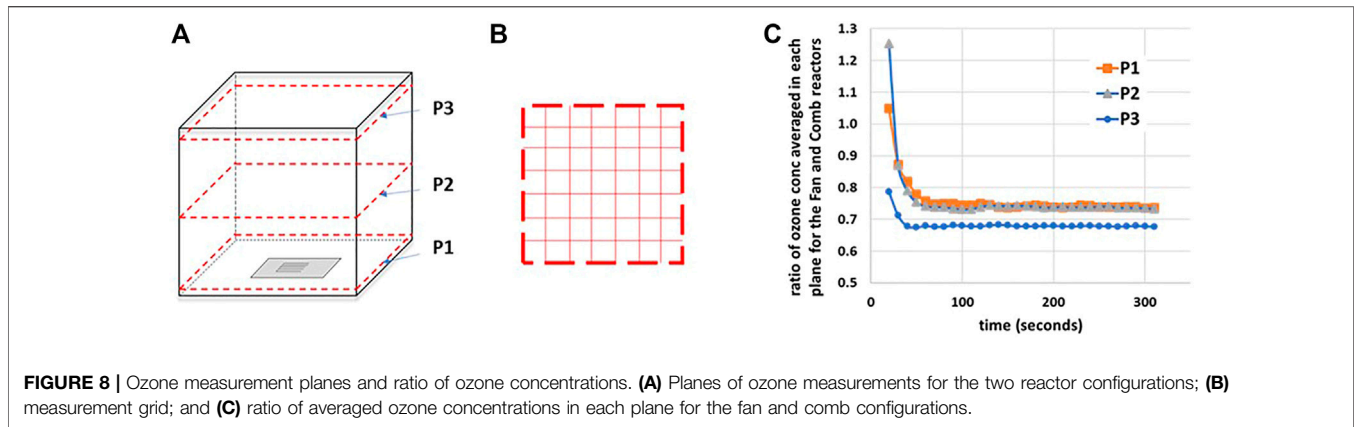## 3.2 SDBD Actuated Ozone Distribution Affecting Decontamination Distribution

Ozone generated and distributed by the two reactors was studied for understanding the effect of SDBD actuated ozone distribution on corresponding decontamination distribution. Experimental ozone data collected for three planes (P1, P2, and P3) inside the chamber in a 6×6 measurement grid over 5 min (Figure 8A) are discussed next.

The ozone data showed that the fan reactor had slightly less concentrations at the measurement points when compared to the comb reactor. Further inspection led to an interesting observation: the ratio of ozone concentrations at each time point, for 5 min with a time step of 10 s, averaged over the grid points in a plane for the fan and comb reactors was found to be nearly constant at 0.76 for P1 and P2 and 0.69 for P3 after 40 s of powering the reactor (Figure 8C). This ozone concentration ratio at one time point is the ratio of the plane averaged concentration generated by the fan reactor to that generated by the comb reactor at that time point. The ozone concentration ratios for the fan vs comb configuration were found to be approximately equal to the ratio of the area covered by the plasma perimeter formed for each configuration (=0.78). This suggests a possible correlation between ozone generation by the two configurations and their corresponding areas after initial ozone formation and decomposition reactions come to an equilibrium. Although confirmation of this correlation is out of the scope of the current study, the constant ratio for the ozone concentrations of the fan and comb configurations was used to calculate comb-equivalent fan ozone concentration values at each grid point, which is used to obtain fan actuated ozone distribution for comparison of the distribution of ozone by the two reactors.

Figure 9 shows SDBD actuated ozone distribution over planes P2 and P3 by the comb and fan reactors at 3.5 min. Like decontamination distribution, the deviations (σ) in ozone concentrations obtained in the P2 and P3 measurement grid indicate uniformity in the ozone distribution, i.e., higher deviations indicate less uniform distribution. Note that plane P2 best indicates SDBD actuated ozone distribution due to minimal wall-flow interactions based on the distance from the chamber walls. First, the ozone distribution (based on experimental data) in planes P2 and P3 is presented and related to corresponding decontamination distribution in the two planes. This is followed by a discussion of the ozone distribution in plane P1.

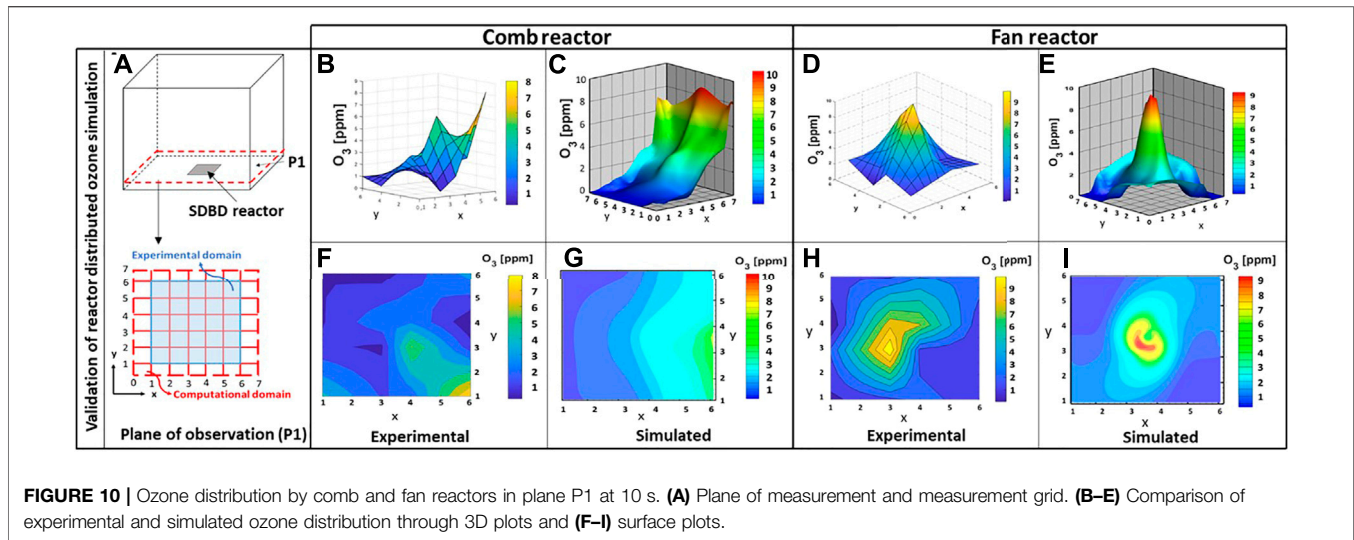### 3.2.1 Ozone Distribution in Plane P2—Experimental

As observed in Figure 9B, the comb reactor resulted in significantly higher concentrations (~215 ppm) along line Q3 compared to points lying in lines Q1 and Q2 (170–190 ppm). This explains the higher microbial reductions (4–5 log) along line Q3 compared to points in line Q1 and Q2 (Figure 7B). The fan reactor resulted in a more uniform ozone distribution

FIGURE 8 | Ozone measurement planes and ratio of ozone concentrations. **(A)** Planes of ozone measurements for the two reactor configurations; **(B)** measurement grid; and **(C)** ratio of averaged ozone concentrations in each plane for the fan and comb configurations.

FIGURE 9 | SDBD actuated ozone distribution in planes P2 and P3 by the comb and fan reactors. **(A,D)** Measurement grid and reactor orientation; **(B,E)** distribution at 3.5 min in plane P2; **(C,F)** distribution at 3.5 min in plane P2. Here, O_3 (min) and O_3 (max): minimum and maximum ozone concentrations (ppm) achieved in each plane, respectively. σ refers to deviation of the concentrations over the plane, indicating uniformity in ozone distribution.

(186–202 ppm) with slightly lower reductions at the corner points as seen in **Figure 9E**. This explains the uniform decontamination distribution resulting from the fan reactor as seen in **Figure 7D**. Observing the ozone distribution and decontamination distribution caused by the two reactors (**Figures 7**, **9**) shows the effect of spatial distribution of ozone concentrations on that of resulting decontamination. In other words, SDBD actuated decontamination distribution can be explained by SDBD actuated ozone distribution.

Standard deviations in the mean of normalized log reductions and ozone concentrations obtained in the measurement grids are used to quantitatively relate ozone distribution and decontamination distribution. Higher deviations indicate less uniform distribution. For the comb reactor, the deviations of the mean log reductions and ozone concentrations were found to be 0.76 and 8.1 ppm, respectively, while the fan reactor resulted in corresponding deviations of 0.35 and 5 ppm. The deviations in ozone concentrations and mean log reductions can be used as a measure of uniformity of ozone available for disinfection in a plane and can be connected to maximum utilization of the reactor-generated ozone in the chamber. Going back to the example of a surface to be disinfected by the comb reactor

FIGURE 10 | Ozone distribution by comb and fan reactors in plane P1 at 10 s. **(A)** Plane of measurement and measurement grid. **(B–E)** Comparison of experimental and simulated ozone distribution through 3D plots and **(F–I)** surface plots.

were to be placed in P2, it would receive higher ozone concentrations in some regions compared to others for the exposure time of 3.5 min resulting in uneven disinfection. For complete disinfection of the contaminated surface, increased exposure times (>3.5 min) and overall ozone dosage will be required. In comparison, the surface in P2 would be disinfected more uniformly by the fan reactor for the exposure time of 3.5 min due to uniformity in ozone available, i.e., effective utilization of generated ozone will take place due to better distribution.

3.2.2 Ozone Distribution in Plane P3—Experimental
Figures 9C,F show the ozone distributions obtained for the two reactor configurations in plane P3 and can be related to corresponding decontamination distributions shown in **Figures 7C,E**. Since P3 is very close to the top chamber wall, the distribution obtained here has significant effects of the wall. This can be used to explain the difference in ozone distribution trends between the two planes for both reactor configurations. Even so, **Figure 9** shows better ozone distribution generated by the fan configuration. In plane P3, deviations in ozone concentrations for comb and fan reactors were found to be 4.4 and 3.09 ppm, respectively. Corresponding deviations in microbial log reduction for comb and fan reactors were found to be 0.71 and 0.48, respectively.

3.2.3 Ozone Distribution in Plane P1—Experimental and Numerically Simulated
This section discusses the initial (10-s postpowering the reactors) ozone distribution by the two reactors at plane P1 studied both experimentally and numerically to get a better understanding of actuated ozone distribution. For the ozone and flow simulations, the mesh was highly refined at the reactor surfaces and 5 cm in each direction around it to capture flow structures that formed

near the reactor surface. A mesh independence study was performed to determine a computationally efficient but accurate mesh size. Three different meshes were tested by refining the coarsest mesh using the mesh refinement feature in Ansys Fluent. The numbers of grid points corresponding to these meshes were 238,216, 373,567, and 565,779. The maximum error of the calculated values over the computational domain, defined as the difference from the finest mesh, was used to compare the meshes. The mesh with 373,567 grid points was selected as it resulted in a maximum error of less than 10^{-5} and 10^{-8} for velocity (m/s) and ozone concentrations (ppb), respectively.

Figures 10A–I compare experimental and numerically simulated SDBD actuated ozone distribution in plane P1 after 10 s of powering up the reactors. The simulated data are verified and validated through the comparison of experimental and simulated 3D and surface plots along with percentage differences between the peak concentrations achieved.

Figure 10B (experimental) and **Figure 10C** (simulated) show that the comb reactor results in higher ozone concentrations near one wall of the chamber due to the dominant wall jet along the comb teeth (**Figure 11**). Note that the computational domain includes ozone data at the walls unlike the experimental domain (**Figure 10A**). Thus, simulated peak concentrations are higher than experimental peaks due to higher concentrations at the wall where the wall jet hits the chamber. The percentage difference between the peak concentrations observed in experimental and computational data for the comb reactor was found to be 8.5%. For better comparison, surface plots of numerical and experimental ozone distribution by the comb reactor in the experimental domain are shown in **Figures 10F,G**. The simulated ozone distribution is observed to be more symmetric along the shaft compared to the experimental data and can be explained by experimental bias in sampling.
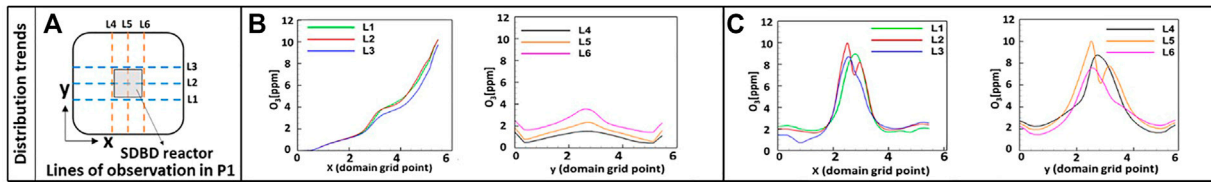
FIGURE 11 | Comparison of simulated ozone distribution trends by comb and fan reactors along 6 lines in plane P1 at 10 s. **(A)** Reactor placement and lines of measurement. **(B)** Ozone distribution trends by the comb reactor. **(C)** Ozone distribution trends by the fan reactor.
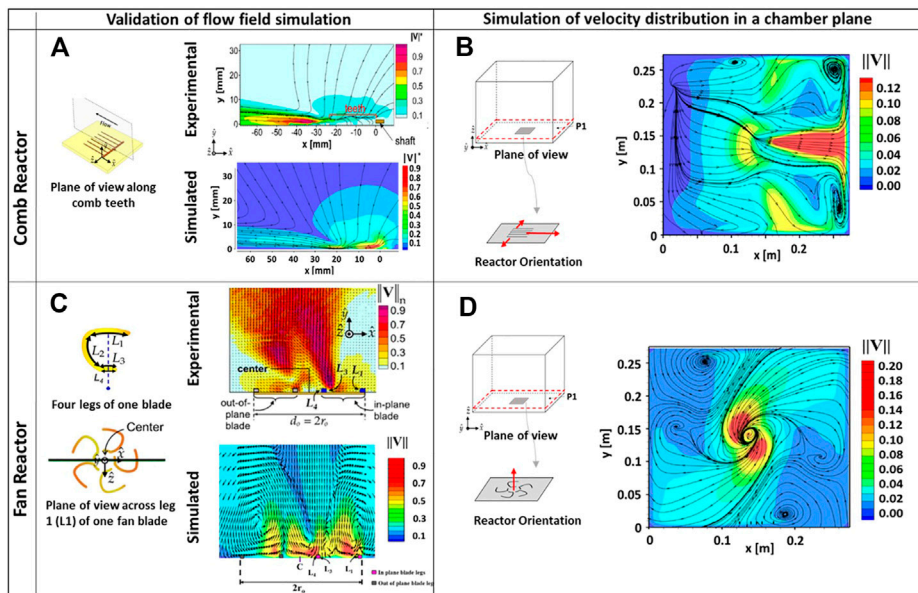
FIGURE 12 | Flow actuation distribution by comb and fan reactors in plane P1 at 10 s. **(A,C)** Validation of simulated data with experimental data [23] and **(B,D)** simulated velocity distribution in plane P1 inside the experimental chamber of size 0.273 m × 0.273 m × 0.286 m.

In comparison to the comb reactor, **Figures 10D–I** show that the fan reactor results in higher concentrations at the center of P1 suggesting a more uniform distribution through the chamber with time. Since the fan reactor results in peak concentration at the center of P1, the numerical and experimental peaks match even though the computational domain includes additional wall data as seen in **Figures 10H,I**. A shift of 1.8 cm in the numerical and experimental peak concentration points in both directions can be attributed to experimental bias during sampling. The percentage difference between the numerical and experimental peak concentrations for the fan reactor was found to be 4%.

Ozone distribution was also simulated along different lines in plane P1 at 10 s to understand the distribution characteristics of the two configurations at the plane near the reactor surface, shown in **Figure 11**. The ozone distribution along these lines across the plane shows a uniform distribution of the ozone generated by the fan reactor in all directions from the center.

In contrast, the comb shows a biased distribution toward only one direction from the center.

3.3 SDBD Configurations to Actuate Flow for Ozone Distribution and Targeted Decontamination

Flow actuation by the two SDBD reactors was simulated to understand the effect of SDBD actuated flow on ozone distribution. Since reactor configurations can be designed based on desired flow patterns, relating simulated SDBD flow actuation to corresponding ozone distribution and resulting decontamination distribution can provide a tool for designing reactor configurations for desired decontamination distribution, i.e., targeted decontamination.

Simulated flow fields near the reactor surface were validated with existing experimental data prior to simulating SDBD actuated flow distribution in the chamber planes. **Figures**

12A,C show validation of the simulated flow fields generated by the comb and fan reactors. The simulation results match the experimental data [23] showing a) the dominant wall jet along the comb teeth from the shaft to the teeth tips, for the comb reactor, and b) the conical rotating upward jet spreading radially outward, for the fan reactor. The simulated vector field matches with experimental data with difference in the contours due to difference in peak velocity regions caused by error in PIV (particle image velocimetry) generated experimental data near the plasma area. The PIV error is due to the interaction between seeding particles and local electric fields [52, 53] resulting in lower velocities to be observed in the plasma area. Thus, experimental peak velocities are observed at the plasma boundaries, while the simulated peaks appear in the plasma area.

After validation of the simulated flow fields, velocity distribution by the reactors in plane P1 of the test chamber was simulated to understand its effect on SDBD actuated ozone and decontamination distribution. The top view of the velocity distribution resulting from the comb reactor flow actuation (see **Figure 12B**) shows three wall jets including the dominant wall jet along the teeth. The contribution of the chamber walls in comb reactor actuated flow distribution is also seen here. **Figure 12D** shows the velocity vector distribution generated by the fan reactor in P1 of the test chamber and gives the top view of the conical rotating upward jet. Compared to the comb reactor, the fan reactor results in a more distributed flow field extending along all three axes (3D) in comparison to the comb reactor generated flow field, which extends mostly along two axes (2D) parallel to the reactor surface. Similar trends are reflected in the ozone distribution resulting from the two reactors shown in **Figure 6**.

The velocity distribution and corresponding ozone distribution at plane P1 of the two reactors at 10 s of powering up the reactor shown in **Figures 10**, **12** can be used to explain ozone and decontamination distribution achieved by the two reactors in planes P2 and P3 of the chamber shown in **Figures 7**, **9**. The comb reactor velocity distribution is biased toward one wall resulting in biased ozone and decontamination distribution, while the fan results in a swirl flow uniformly distributing ozone from the center toward all the walls. Furthermore, the contribution of the chamber walls in ozone distribution is more significant for the comb reactor compared to the fan reactor. Comparing SDBD actuated ozone distribution and flow field distribution also suggests that convection is more significant than diffusion in the transport of DBD-generated species when the electrodes are designed for flow actuation. Simulated ozone concentrations along 6 lines in P1 shown in **Figure 11** further illustrate the difference between ozone distribution characteristics of the two reactors caused by the difference in design configurations. This signifies the ability of SDBD electrode designs for controlled SDBD actuated ozone distribution for targeted decontamination. Thus, an experiment integrated computationally inexpensive numerical simulation method like the one used in this study can be used for designing SDBD reactors for targeted decontamination using commercially available CFD software in conjunction with

SDBD body force distribution models and experimental ozone generation and decomposition rates available in literature [24, 25].

3.4 Relation Between Distribution of Local Decontamination and Local Ozone Concentrations Inside an Enclosure

To relate local ozone concentrations and resulting decontamination, the experimental data were used to test the research hypothesis that local decontamination achieved at a point inside a chamber and corresponding ozone concentration reaching that point are positively correlated. In other words, local decontamination increases with increment in available ozone at a fixed point inside the enclosure. Thus, the null and alternate hypotheses tested are H_0: $\rho \leq 0$ and H_A: $\rho > 0$, respectively, as explained in *Statistical Analysis*. The two variables tested are the mean of normalized log reduction ($\overline{L_n}$) at a spatial point inside the chamber and total ozone concentrations reaching that point (O_{3CT}). $\overline{L_n}$ is the mean of the normalized log reductions achieved from 5 repeats at each point after 3.5 min of exposure as explained before. Total ozone concentrations reaching a point, O_{3CT}, is denoted by the ozone CT (concentration x time) value calculated at that point. ρ was calculated based on 36 samples: nine points for 2 planes with 2 reactors. Note that the reactor configuration does not matter in this analysis since we are testing the correlation between local decontamination and local ozone concentrations, which does not depend on the generation source of ozone concentrations. Pearson's correlation value was found to be ρ [34] = 0.64 > 0 with $p < 0.001$. ρ [34] >0 implies that the null hypothesis can be rejected, i.e., there exists a positive correlation between the tested variables. A low p-value (<0.001) establishes that there is a significant positive relationship between local decontamination achieved at a point inside a chamber and corresponding ozone concentration reaching that point.

4 DISCUSSION

The implications of the decontamination distribution results can be understood by the example of placing a contaminated surface that needs to be disinfected by SDBD exposure in P2 or P3 inside the chamber. The comb reactor would disinfect it unevenly for the exposure time of 3.5 min and require longer exposure for disinfection of certain regions of the surface. In comparison, the fan reactor would disinfect the surface evenly in 3.5 min without requiring extra exposure. In other words, the fan reactor would result in higher overall disinfection of the surface than the comb reactor for the same exposure time when run at equal power levels. The deviations in ozone concentrations can be used as a measure of uniformity of ozone available for disinfection in a plane and can be connected to maximum utilization of the reactor-generated ozone in the chamber. For the example of the contaminated surface placed in P2 or P3, the comb reactor will result in biased distribution of ozone generated in 3.5 min resulting in uneven disinfection of the surface for that exposure time. For complete disinfection of the contaminated surface,

increased exposure times, and global ozone concentrations, ozone dosage will be required. In comparison, the fan reactor will result in uniform distribution of the ozone generated and evenly decontaminate the surface within 3.5 min. Thus, when compared to the comb reactor, the fan reactor results in more effective utilization of the generated ozone for the disinfection of a surface (or surfaces of an object) placed in planes P2 and P3 of the chamber for an exposure time of 3.5 min due to better ozone distribution resulting in higher overall surface disinfection. More effective utilization of ozone over the SDBD exposure period represents lower ozone dosage required for obtaining the desired disinfection levels. Additionally, higher overall surface disinfection obtained for a given SDBD exposure time means lower energy (power × time) requirements for obtaining the desired disinfection. Thus, SDBD actuated decontamination can be used to achieve targeted decontamination with efficient utilization of ozone for obtaining the desired disinfection for a given period by controlling the ozone distribution. Furthermore, smart decontamination can be achieved by using surface sensors to identify the target areas, i.e., the desired areas to be decontaminated. The above results-based comparison of the comb and fan reactors for the disinfection of a surface placed in planes P2 and P3 of the chamber in 3.5 min can be generalized as follows: SDBD actuated decontamination distribution can be used to achieve smart or targeted decontamination resulting in lower exposure times, ozone dosage requirements, and energy requirements for the desired disinfection.

For practical utilization of this concept, SDBD actuated decontamination distribution needs to be related to SDBD reactor design configurations. Furthermore, this relation should be based on data obtainable through time-efficient and economical methods. For this purpose, an experiment integrated numerical simulation method, based on SDBD body force distribution models and experimental ozone generation and decomposition rates available in literature, can be used to predict SDBD actuated ozone distribution and resulting decontamination distribution. Such a model was used to simulate the initial ozone distribution caused by the fan and comb reactors at plane P1 and matched with corresponding experimental data. Since reactor configurations can be designed based on the desired flow patterns, relating simulated SDBD flow actuation to resulting ozone and decontamination distribution provides a tool for designing reactor configurations for targeted decontamination. The simulated velocity distribution and corresponding ozone distribution at plane P1 resulting from the two reactors explained the biased ozone and decontamination distribution in P2 and P3 formerly discussed. Comparing SDBD actuated ozone distribution and flow field distribution also suggested that convection is more significant than diffusion in the transport of DBD-generated species when the electrodes are designed for flow actuation.

This research introduces the concept of synergistic employment of flow actuation and ozone generation by SDBD reactors to simultaneously generate and distribute ozone for targeted decontamination. Targeted decontamination maximizes ozone utilization resulting in lower ozone dosage, energy consumption, and exposure times required for decontamination. This can have considerable implications in

designing smart and efficient SDBD decontamination systems for food preservation and sterilization of advanced materials used in electronics and spacecraft components, which can benefit from an inbuilt customizable distributing agent in the ozone generation device without increment in capital for doing so.

5 CONCLUSION

SDBD actuated decontamination distribution was examined inside an enclosure and its relation to SDBD-generated ozone distributed by SDBD flow actuation resulting from selected reactor configurations was established. Two SDBD reactor designs with contrasting flow actuation patterns were considered for this study: the comb reactor and the fan reactor. Decontamination distribution was obtained by measuring reduction in logs of bacterial CFUs on contaminated coupons placed in distributed points lying in two planes inside a chamber: P2 (central plane) and P3 (plane near the top of the chamber), caused by exposure to the SDBD reactors run at a power of 1 W for 3.5 min. Ozone distribution caused by the two reactors run at the same power was also measured at P2 and P3. The deviations (σ) in the mean of normalized log reductions and ozone measurements over a plane were used to indicate uniformity in decontamination and ozone distribution, respectively, i.e., higher deviations indicate less uniform distribution. In both the planes, the comb reactor resulted in a biased decontamination (σ: P2 = 0.76, P3 = 0.71) and ozone (σ: P2 = 8.1 ppm, P3 = 4.4 ppm) distribution, while the fan reactor resulted in a more uniform decontamination (σ: P2 = 0.35, P3 = 0.48) and ozone (σ: P2 = 5 ppm, P3 = 3.1 ppm) distribution. Additionally, initial ozone distribution caused by the fan and comb reactors was experimentally measured at an additional plane P1 inside the same chamber and matched with corresponding simulated data based on SDBD body force distribution models and experimental ozone generation and decomposition rates available in literature. Lastly, a bivariate statistical analysis was performed to relate local decontamination and local ozone concentrations inside an enclosure that showed a significant positive correlation with Pearson's correlation, ρ [34] = 0.64 with $p < 0.001$.

The first conclusion of this study is that ozone generation and flow actuation capabilities of SDBD reactors can be synergistically applied to achieve SDBD actuated decontamination. The spatial distribution in local decontamination levels achieved by fan and comb reactors shows the application of SDBD actuated decontamination for targeted decontamination of desired surface areas in lower exposure times by maximizing ozone utilization. Maximizing ozone utilization results in lowering ozone dosage requirements, while lower exposure times result in lower energy consumption by the reactors running at the same power. Additionally, smart decontamination can be achieved by using surface sensors to control SDBD targeted decontamination. The second conclusion of this study is that SDBD reactors can be designed using experiment integrated numerical simulation methods to predict targeted decontamination. This is based on the results demonstrating the

use of reactor configurations, SDBD force distribution models, and experimental ozone generation data to simulate SDBD ozone distribution for targeted decontamination. Lastly, it is concluded that local decontamination and local ozone concentrations inside an enclosure have a significant positive correlation. The significant positive correlation can be extended to all ozone generators beyond DBD reactors for targeted decontamination. Since our results are focused on ozone distribution and its spatial antimicrobial efficacy, a thorough study of other RONS species is needed soon.

DATA AVAILABILITY STATEMENT

The original contributions presented in the study are included in the article/**Supplementary Material**; further inquiries can be directed to the corresponding author.

AUTHOR CONTRIBUTIONS

BC and SR contributed to the conception and design of the study. BC, JJ, SP, and SR contributed to the development of the methodology. BC, SP, and EM collected and organized the data. BC performed the statistical analysis. BC wrote the first draft of the manuscript. All authors contributed to manuscript revision, read, and approved the submitted version.

SUPPLEMENTARY MATERIAL

The Supplementary Material for this article can be found online at: https://www.frontiersin.org/articles/10.3389/fphy.2022.834030/full#supplementary-material

REFERENCES

1. Scholtz V, Pazlarova J, Souskova H, Khun J, Julak J, Nonthermal Plasma - A Tool for Decontamination and Disinfection. *Biotechnol Adv* (2015) 33(6): 1108–19. doi:10.1016/j.biotechadv.2015.01.002

2. Ghomi H, Mohades S, Navab Safa N, Dabiri H Surface Decontamination by Dielectric Barrier Discharge Plasma. *J Biomed Phys Eng* (2012) 2(2):72.

3. Ecss-Q-St-70-53C. *ECSS-Q-ST-70-53C Materials and Hardware Compatibility Tests for Sterilization Processes*. Noordwijk, Netherlands: European Cooperation for Space Standardization (2008).

4. Mandal R, Singh A, Pratap Singh A Recent Developments in Cold Plasma Decontamination Technology in the Food Industry. *Trends Food Sci Techn* (2018) 80:93–103. doi:10.1016/j.tifs.2018.07.014

5. Fekadu S, Merid Y, Beyene H, Teshome W, Gebre-Selassie S Assessment of Antibiotic- and Disinfectant-Resistant Bacteria in Hospital Wastewater, South Ethiopia: a Cross-Sectional Study. *J Infect Dev Ctries* (2015) 9(02):149–56. doi:10.3855/jidc.4808

6. Moreau M, Orange N, Feuilloley MGJ Non-thermal Plasma Technologies: New Tools for Bio-Decontamination. *Biotechnol Adv* (2008) 26(6):610–7. doi:10.1016/j.biotechadv.2008.08.001

7. Schuerger AC, Trigwell S, Calle CI Use of Non-thermal Atmospheric Plasmas to Reduce the Viability ofBacillus Subtilison Spacecraft Surfaces. *Int J Astrobiology* (2008) 7(1):47–57. doi:10.1017/s1473550407004016

8. Tanino M, Xilu W, Takashima K, Katsura S, Mizuno A Sterilization Using Dielectric Barrier Discharge at Atmospheric Pressure. *Int J Plasma Environ Sci Techn* (2007) 1(1):102–7. doi:10.34343/ijpest.2007.01.01.102

9. Kogelschatz U Dielectric-barrier Discharges: Their History, Discharge Physics, and Industrial Applications. *Plasma Chem plasma Process* (2003) 23(1):1–46. doi:10.1023/a:1022470901385

10. Park S-L, Moon J-D, Lee S-H, Shin S-Y Effective Ozone Generation Utilizing a Meshed-Plate Electrode in a Dielectric-Barrier Discharge Type Ozone Generator. *J Electrostatics* (2006) 64(5):275–82. doi:10.1016/j.elstat.2005.06.007

11. Balzer J, Heuer K, Demir E, Hoffmanns MA, Baldus S, Fuchs PC, et al. Non-thermal Dielectric Barrier Discharge (DBD) Effects on Proliferation and Differentiation of Human Fibroblasts Are Primary Mediated by Hydrogen Peroxide. *PLoS One* (2015) 10:e0144968–12. doi:10.1371/journal.pone.0144968

12. Vatansever F, de Melo WCMA, Avci P, Vecchio D, Sadasivam M, Gupta A, et al. Antimicrobial Strategies Centered Around Reactive Oxygen Species - Bactericidal Antibiotics, Photodynamic Therapy, and beyond. *FEMS Microbiol Rev* (2013) 37(6):955–89. doi:10.1111/1574-6976.12026

13. Pavlovich MJ, Ono T, Galleher C, Curtis B, Clark DS, Machala Z, et al. Air Spark-like Plasma Source for Antimicrobial NOxgeneration. *J Phys D: Appl Phys* (2014) 47(50):505202. doi:10.1088/0022-3727/47/50/505202

14. Laroussi M, Leipold F Evaluation of the Roles of Reactive Species, Heat, and UV Radiation in the Inactivation of Bacterial Cells by Air Plasmas at Atmospheric Pressure. *Int J Mass Spectrom* (2004) 233(1-3):81–6. doi:10.1016/j.ijms.2003.11.016

15. Mastanaiah N, Banerjee P, Johnson JA, Roy S Johnson, and Subrata RoyExamining the Role of Ozone in Surface Plasma Sterilization Using Dielectric Barrier Discharge (DBD) Plasma. *Plasma Process Polym* (2013) 1012:1120–33. doi:10.1002/ppap.201300108

16. Kim CK, Gentile DM, Sproul OJ Mechanism of Ozone Inactivation of Bacteriophage F2. *Appl Environ Microbiol* (1980) 39(1):210–8. doi:10.1128/aem.39.1.210-218.1980

17. Victorin K Review of the Genotoxicity of Ozone. *Mutat Research/Reviews Genet Toxicol* (1992) 277(3):221–38. doi:10.1016/0165-1110(92)90045-b

18. Burleson GR, Murray TM, Pollard M Inactivation of Viruses and Bacteria by Ozone, with and without Sonication. *Appl Microbiol* (1975) 29(3):340–4. doi:10.1128/am.29.3.340-344.1975

19. Thanomsub B, Anupunpisit V, Chanphetch S, Watcharachaipong T, Poonkhum R, Srisukonth C Effects of Ozone Treatment on Cell Growth and Ultrastructural Changes in Bacteria. *J Gen Appl Microbiol* (2002) 48(4): 193–9. doi:10.2323/jgam.48.193

20. Kim J-G, Yousef AE, Dave S Application of Ozone for Enhancing the Microbiological Safety and Quality of Foods: a Review. *J Food Prot* (1999) 62(9):1071–87. doi:10.4315/0362-028x-62.9.1071

21. Choudhury B, Portugal S, Mastanaiah N, Johnson JA, Roy S. Inactivation of *Pseudomonas aeruginosa* and Methicillin-Resistant Staphylococcus aureus in an Open Water System with Ozone Generated by a Compact, Atmospheric DBD Plasma Reactor. *Sci Rep* (2018) 8(1):17573–11. doi:10.1038/s41598-018-36003-0

22. Eto H, Ono Y, Ogino A, Nagatsu M Low-temperature Sterilization of Wrapped Materials Using Flexible Sheet-type Dielectric Barrier Discharge. *Appl Phys Lett* (2008) 93(22):221502. doi:10.1063/1.3039808

23. Portugal S, Choudhury B, Lilley A, Charters C, Porrello C, Lin J, et al. A Fan-Shaped Plasma Reactor for Mixing Enhancement in a Closed Chamber. *J Phys D: Appl Phys* (2020) 53(22):22LT01. doi:10.1088/1361-6463/ab7e64

24. Singh KP, Roy S Force Generation Due to Three-Dimensional Plasma Discharge on a Conical Forebody Using Pulsed Direct Current Actuators. *J Appl Phys* (2008) 103(10):103303. doi:10.1063/1.2924422

25. Portugal S, Roy S, Lin J. Functional Relationship between Material Property, Applied Frequency and Ozone Generation for Surface Dielectric Barrier Discharges in Atmospheric Air. *Sci Rep* (2017) 7(1):6388–11. doi:10.1038/s41598-017-06038-w

26. Benard N, Moreau E Role of the Electric Waveform Supplying a Dielectric Barrier Discharge Plasma Actuator. *Appl Phys Lett* (2012) 100(19):193503. doi:10.1063/1.4712125

27. Benard N, Moreau E. Electrical and Mechanical Characteristics of Surface AC Dielectric Barrier Discharge Plasma Actuators Applied to Airflow Control. *Experiments in Fluids* (2014) 55(11):1–43. doi:10.1007/s00348-014-1846-x

28. Leonov SB, Adamovich IV, Soloviev VR Dynamics of Near-Surface Electric Discharges and Mechanisms of Their Interaction with the Airflow. *Plasma Sourc Sci. Technol.* (2016) 25(6):063001. doi:10.1088/0963-0252/25/6/063001

29. Enloe CL, Font GI, McLaughlin TE, Orlov DM Surface Potential and Longitudinal Electric Field Measurements in the Aerodynamic Plasma Actuator. *AIAA J* (2008) 46(11):2730–40. doi:10.2514/1.33973

30. Tirumala R, Benard N, Moreau E, Fenot M, Lalizel G, Dorignac E Temperature Characterization of Dielectric Barrier Discharge Actuators: Influence of Electrical and Geometric Parameters. *J Phys D: Appl Phys* (2014) 47(25):255203. doi:10.1088/0022-3727/47/25/255203

31. Thomas FO, Corke TC, Iqbal M, Kozlov A, Schatzman D Optimization of Dielectric Barrier Discharge Plasma Actuators for Active Aerodynamic Flow Control. *AIAA J* (2009) 47(9):2169–78. doi:10.2514/1.41588

32. Shimizu S, Barczyk S, Rettberg P, Shimizu T, Klaempfl T, Zimmermann JL, et al. Cold Atmospheric Plasma - A New Technology for Spacecraft Component Decontamination. *Planet Space Sci* (2014) 90:60–71. doi:10.1016/j.pss.2013.10.008

33. Walsh DM, Hokenstad AN, Chen J, Sung J, Jenkins GD, Chia N, et al. Postmenopause as a Key Factor in the Composition of the Endometrial Cancer Microbiome (ECbiome). *Sci Rep* (2019) 9(1):19213–6. doi:10.1038/s41598-019-55720-8

34. Cytiva Whatman. (2021).Cytiva Whatman™ Quantitative Filter Paper: Grade 42 Circles (Cytiva, Catalog No.09-855B)

35. Spordex Biological Indicator Discs (2021). Available at: https://www.sterislifesciences.com/products/biological-and-chemical-indicators/biological-indicators/spordex-discs.

36. 2B Technologies, Inc. "Model 202 Ozone Monitor Manual" (2B Technologies" (2001). Available at: https://twobtech.com/docs/manuals/model_202_revJ.pdf.

37. Ansys Fluent. *ANSYS FLUENT Theory Guide.* Canonsburg, PA: ANSYS, Inc (2018).

38. Gupta AD, Roy S Three-dimensional Plasma Actuation for Faster Transition to Turbulence. *J Phys D: Appl Phys* (2017) 50(42):425201. doi:10.1088/1361-6463/aa8879

39. Choudhury B, Portugal S, Johnson J, Roy S. *Performance Evaluation of Fan and Comb Shaped Plasma Reactors for Distribution of Generated Ozone in a Confined Space.* Orlando, FL: AIAA Scitech 2020 Forum (2020). p. 1165. doi:10.2514/6.2020-1165

40. Devins JC Mechanism of Ozone Formation in the Silent Electric Discharge. *J Electrochem Soc* (1956) 103(8):460. doi:10.1149/1.2430380

41. Gibalov VI, Samoilovich VG, Filippov Yu V Physical Chemistry of the Electrosynthesis of Ozone. The Results of Numerical Experiments. *Russ J Phys Chem* (1981) 55:471–9.

42. Sabersky RH, Sinema DA, Shair FH Concentrations, Decay Rates, and Removal of Ozone and Their Relation to Establishing Clean Indoor Air. *Environ Sci Technol* (1973) 7(4):347–53. doi:10.1021/es60076a001

43. Yagi S, Tanaka M Mechanism of Ozone Generation in Air-Fed Ozonisers. *J Phys D: Appl Phys* (1979) 12(9):1509–20. doi:10.1088/0022-3727/12/9/013

44. Eliasson B, Hirth M, Kogelschatz U Ozone Synthesis from Oxygen in Dielectric Barrier Discharges. *J Phys D: Appl Phys* (1987) 20(11):1421–37. doi:10.1088/0022-3727/20/11/010

45. Altshuller AP Measurements of the Products of Atmospheric Photochemical Reactions in Laboratory Studies and in Ambient Air-Relationships between Ozone and Other Products. *Atmos Environ (1967)* (1983) 17(12):2383–427. doi:10.1016/0004-6981(83)90066-5

46. Blanchard CL Ozone Process Insights from Field Experiments–Part III: Extent of Reaction and Ozone Formation. *Atmos Environ* (2000) 34:122035–42043. doi:10.1016/s1352-2310(99)00458-6

47. Ito K Experimental and CFD Analyses Examining Ozone Distribution in Model Rooms with Laminar and Turbulent Flow fields. *J Asian Architecture Building Eng* (2007) 6(2):387–94. doi:10.3130/jaabe.6.387

48. Gurol MD, Singer PC Kinetics of Ozone Decomposition: a Dynamic Approach. *Environ Sci Technol* (1982) 16(7):377–83. doi:10.1021/es00101a003

49. Benson SW, Arthur EA Mechanism of the Gas Phase, thermal Decomposition of Ozone. *J Chem Phys* (1957) 26(6):1718. doi:10.1063/1.1743610

50. Glissmann A, Schumacher HJ Der Thermische Ozonzerfall. *Z für Physikalische Chem* (1933) 21(1):323–48. doi:10.1515/zpch-1933-2130

51. Takeshita T, Kageyama S, Furuta M, Tsuboi H, Takeuchi K, Shibata Y, et al. Bacterial Diversity in Saliva and Oral Health-Related Conditions: the Hisayama Study. *Sci Rep* (2016) 6(1):22164–11. doi:10.1038/srep22164

52. Masati A, Sedwick RJ Electrostatic Forces Acting on Particle Image Velocimetry Tracer Particles in a Plasma Actuator Flow. *J Appl Phys* (2018) 123(1):014904. doi:10.1063/1.4998407

53. Hamdi M, Havet M, Rouaud O, Tarlet D Comparison of Different Tracers for PIV Measurements in EHD Airflow. *Experiments in fluids* (2014) 55(4):1–12. doi:10.1007/s00348-014-1702-z